High Power Laser Science and Engineering, (2025), Vol. 13, e3, 17 pages.
doi:10.1017/hpl.2024.85

HIGH POWER LASER SCIENCE AND ENGINEERING

RESEARCH ARTICLE

Advanced plasma target from pre-ionized low-density foam for effective and robust direct laser acceleration of electrons

Olga N. Rosmej[1,2,3], Mikhail Gyrdymov[2], Nikolay E. Andreev[4,5], Parysatis Tavana[2,6], Vyacheslav Popov[4], Nataliya G. Borisenko[7], Alexandr I. Gromov[7], Sergey Yu. Gus'kov[7], Rafael Yakhin[7], Galina A. Vegunova[7], Nikolai Bukharskii[7,8], Philipp Korneev[7,8], Jakub Cikhardt[9], Sero Zähter[2,10], Sebastian Busch[2], Joachim Jacoby[2,3], Vladimir G. Pimenov[11], Christian Spielmann[6], and Alexander Pukhov[12]

[1] *GSI Helmholtzzentrum für Schwerionenforschung GmbH, Darmstadt, Germany*

[2] *Goethe University, Frankfurt, Germany*

[3] *Helmholtz Forschungsakademie Hessen für FAIR, Frankfurt, Germany*

[4] *Joint Institute for High Temperatures, RAS, Moscow, Russia*

[5] *Moscow Institute of Physics and Technology (State University), Dolgoprudny, Russia*

[6] *Institute of Optics and Quantum Electronics (IOQ), University Jena, Jena, Germany*

[7] *P.N. Lebedev Physical Institute RAS, Moscow, Russia*

[8] *National Research Nuclear University MEPhI, Moscow, Russia*

[9] *Faculty of Electrical Engineering, Czech Technical University in Prague, Prague 6, Czech Republic*

[10] *Focused Energy GmbH, Darmstadt, Germany*

[11] *N.D. Zelinsky Institute for Organic Chemistry RAS, Moscow, Russia*

[12] *Heinrich-Heine-University Düsseldorf, Düsseldorf, Germany*

(Received 23 July 2024; revised 14 November 2024; accepted 18 November 2024)

Abstract

Low-density polymer foams pre-ionized by a well-controlled nanosecond pulse are excellent plasma targets to trigger direct laser acceleration (DLA) of electrons by sub-picosecond relativistic laser pulses. In this work, the influence of the nanosecond pulse on the DLA process is investigated. The density profile of plasma generated after irradiating foam with a nanosecond pulse was simulated with a two-dimensional hydrodynamic code, which takes into account the high aspect ratio of interaction and the microstructure of polymer foams. The obtained plasma density profile was used as input to the three-dimensional particle-in-cell code to simulate energy, angular distributions and charge carried by the directional fraction of DLA electrons. The modelling shows good agreement with the experiment and in general a weak dependence of the electron spectra on the plasma profiles, which contain a density up-ramp and a region of near-critical electron density. This explains the high DLA stability in pre-ionized foams, which is important for applications.

Keywords: near critical density plasma; low density foam; direct laser acceleration; super ponderomotive electrons

1. Introduction

Direct laser acceleration (DLA) of electrons in plasma of near-critical electron density (NCD) was predicted in Refs. [1,2] based on three-dimensional (3D) particle-in-cell (PIC) simulations of the relativistic laser pulse interaction with extended pre-plasma. The authors proposed a mechanism of direct laser energy coupling into hot electrons, which requires strong self-generated static electric and magnetic fields that confine fast electrons in the relativistic plasma channel. These electrons undergo transverse betatron oscillations along the laser pulse polarization direction and gain energy efficiently when the betatron frequency becomes close to the Doppler shifted laser frequency[1,2].

In the case of large-scale PW-class lasers and underdense plasmas (e.g., gas-jets), DLA can be a predominant

Correspondence to: O. N. Rosmej, GSI Helmholtzzentrum für Schwerionenforschung GmbH, Planckstraße 1, 64291 Darmstadt, Germany. Email: o.rosmej@gsi.de

mechanism of electron acceleration at ultra-relativistic intensities[3] or works in combination with self-modulated laser wake field acceleration at moderate relativistic laser intensities[4,5].

In laser interaction with solid targets, high-energy tails in the electron energy distribution caused by DLA in the pre-plasma generated by a low amplified spontaneous emission (ASE) contrast of 10^{-4}–10^{-6} have been observed in the NOVA[6], OMEGA EP, Titan[7] and PETAL lasers[8].

In Refs. [9,10], a controlled ns pulse was used to hit a solid foil and generate a mm-long plasma with subcritical density. The interaction of a relativistically intense sub-ps pulse with the expanded plasma plume resulted in a highly effective electron temperature and beam charge.

The application of low-density polymer foams to enhance electron acceleration was demonstrated in Ref. [11], where 250 μm thick foam layers of near-critical and overcritical densities were used. The approximation of the high-energy tail of the measured electron spectra with Maxwellian function led to up to four to five times higher effective electron temperatures than the ponderomotive one for low-density foams, while no effect was observed for highly overcritical densities, for example, 100 mg/cm^3. The drawback of this experiment was that the pre-heating by the ns-ASE was the same for all foam densities.

In experiments at the PHELIX laser facility, a well-controlled ns pulse, matched to the foam density and thickness, was used to convert foams into NCD plasma for interaction with a sub-ps pulse of moderate relativistic intensity. Up to a 10–15-fold increase in the effective temperature and beam charge of accelerated electrons was observed compared to shots on metal foils at high laser contrast[12,13]. It was also shown that in these shots, the effective electron temperature, the maximum of the measured electron energy and the beam charge are higher than for shots on metal foil, with ultra-relativistic intensity of 10^{21} W/cm^2[13]. Full 3D PIC simulations performed for the parameters of the laser-target setup used showed good agreement with the experimental results[12–15].

The high efficiency of the DLA mechanism has been confirmed experimentally[16,17] and theoretically[18-20] also for femtosecond laser pulses of relativistic intensity.

These groundbreaking results pave the way for the application of low-density foams to greatly increase the performance of laser-driven particle and radiation sources.

The pre-plasma engineering to optimize DLA is based on the use of low-density aerogels[21–23], which can be pre-heated by a nanosecond laser pulse or soft X-rays[24,25]. The thermodynamic properties of such a plasma are determined by the propagation of the homogenization wave within the porous substance[26–30]. Experiments using hohlraum X-rays for foam heating showed a high hydrodynamic (HD) stability of foams that start to expand with a delay of 10–15 ns after the X-ray pulse, in contrast to a Mylar film with the same areal density[24]. HD simulations with radiative transfer predicted a very flat distribution of electron density and temperature in the plasma generated by X-ray irradiation of 1 mm thick polymer foams of 2 mg/cm^3 density[31]. All these properties make this type of plasma target very attractive for numerous applications[32].

High-current relativistic beams of DLA electrons have a wide range of applications and can be used to generate a bright betatron source[33–36] of tens of MeV bremsstrahlung in the giant dipole resonance region with record-breaking conversion efficiency and neutrons[13,37,38]. Experiments with pre-ionized foams at the PHELIX laser at a moderate relativistic intensity of 10^{19} W/cm^2 have demonstrated that DLA is a highly robust mechanism. It does not require high laser contrast or high pointing stability, yet it provides well-directed electron beams with energy and charge per steradian larger than in the case of 100 times higher intensity when shooting on conventional metal foil[13].

On the other hand, no DLA was observed for shots on polymer foams with a relativistic PHELIX pulse at high laser contrast and without a ns pulse. The measured electron spectra were similar to those of shots on conventional foils.

Despite great success in foam applications demonstrated in experiments at the PHELIX facility, the parameters of the plasma generated by direct irradiation of low-density polymer foams with ns pulses and their influence on the effective temperature and charge of the DLA beam are not yet sufficiently known.

In this work, the influence of foam pre-ionization by the ns pulse on the generation of beams of super-ponderomotive electrons by relativistic laser pulses is investigated. Two-dimensional (2D) HD simulations of the interaction of a nanosecond laser pulse with a layer of porous matter using the code NUTCY-F[26–30,39] were performed to model the propagation of a heating wave inside the foam target and its transformation into fully homogenized plasma.

The plasma density profile obtained based on the HD simulations was used in 3D PIC simulations to model the properties of the accelerated electrons.

The paper is organized as follows: laser and target parameters together with the experimental setup used are described in Section 2; angle-dependent measurements of the electron and proton spectra for two different ns pulses are presented in Section 3; results of 2D HD simulations of ns pulse interaction with structured foams are discussed in Section 4; 3D PIC simulations considering the experimental geometry and the simulated plasma density profile are shown in Section 5; the discussion and summary are presented in Sections 6 and 7, respectively.

2. Experimental setup

Experiments on the generation of well-collimated high-current DLA electrons with energies far above the

https://doi.org/10.1017/hpl.2024.85 Published online by Cambridge University Press

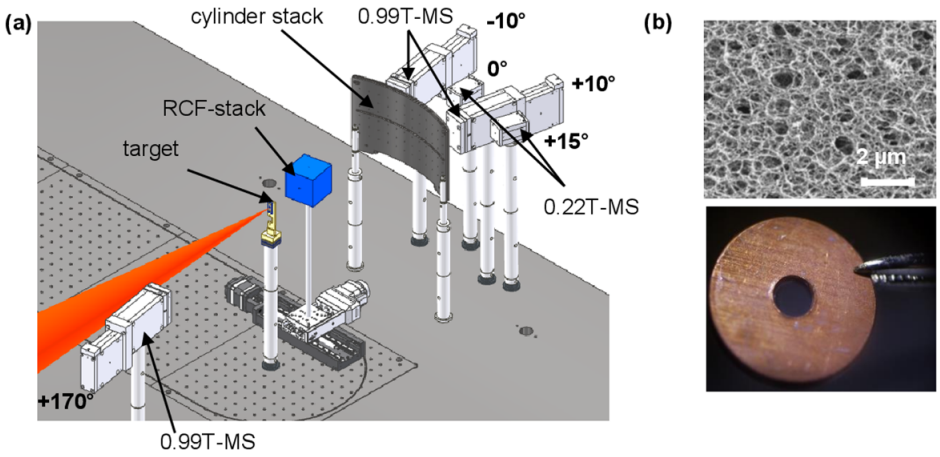

Figure 1. (a) Nanosecond and sub-picosecond PHELIX laser pulses (red) focused by means of 150 cm off-axis parabola on the foam target and diagnostic setup for characterization of electron and proton beams. (b) Optically transparent highly uniform 3D network structure of polymer aerogel and a picture of foam enclosed in a Cu disk.

ponderomotive potential were performed at the Petawatt High Energy Laser for Ion eXperiments (PHELIX) facility at the GSI Helmholtzzentrum in Darmstadt. The S-polarized pulse of the Nd:glass laser with a fundamental wavelength of 1.053 µm and a pulse duration of 750 ± 250 fs[40] was sent to targets at an angle of 3° to the target normal. The laser energy measured after the main amplifier was 80 ± 10 J. This value has to be corrected by the 20% losses in the compressor. After focusing by a 150 cm long off-axis parabolic mirror into an elliptical focal spot with full width at half maximum (FWHM) of (12 ± 2) µm × (14 ± 2) µm, the laser energy on the target E_{FWHM} was approximately equal to 15–20 J and the corresponding laser intensity was (1–2.5) × 10^{19} W/cm^2.

Polymer aerogels consisting of carbon, oxygen and hydrogen (hereinafter referred to as CHO) of 2 mg/cm^3 volume density and 450 ± 50 µm thickness were used as targets[12,21,22]. In terms of areal density, a 400 µm thick foam layer can be compared to a 0.5 µm thin polymer film of 1.4 g/cm^3 density. In the case of fully ionized foam with the chemical composition from Ref. [21], this corresponds to 0.65 × 10^{21} cm^{-3} electron density or 0.65n_{cr}, where the critical electron density is defined as $n_{cr} = \omega^2/(4\pi e^2)$, where m and e are the mass of the electron at rest and its charge, and ω is the laser frequency. In the case of the PHELIX laser, the critical electron density reaches $n_{cr} = 10^{21}$ cm^{-3}.

A sub-mm-long NCD plasma was produced by sending a well-controlled ns pulse forerunning the relativistic main pulse onto a foam. The intensity of the ns laser pulse was varied between 10^{13} and 3×10^{14} W/cm^2, while the delay between ns and sub-ps pulses was between 3 and 5 ns, depending on the foam density and thickness. A 150 cm parabolic mirror with an f/5 number was used to focus ns and sub-ps pulses on the sub-mm-thick foam.

The experimental setup and a low-density polymer aerogel are shown in Figures 1(a) and 1(b). CHO polymer layers are optically transparent and characterized by a highly uniform 3D network structure consisting of sub-µm pores, approximately 40 nm thin fibres with density between 0.1 and 1 g/cm^3. The mean density fluctuations on the focal-spot size area of 100 µm × 100 µm do not exceed 0.5%[23]. Due to their open cell structure, air contained by pores can be evacuated. The foam was grown inside a copper disk (washer) (Figure 1(b)) using a super-critical drying method[21]. Since the foam layer is enclosed in a Cu-washer (Figure 1(b)), it was not possible to measure the electron density profile at the moment of relativistic momentum interaction.

After the action of the ns pulse, the incoming sub-ps relativistic laser pulse generates a relativistic ion channel where a certain number of electrons are ponderomotively expelled from the laser beam with a Gaussian-like intensity profile. Subsequently, in the region with reduced electron density, the remaining electrons undergo transverse betatron oscillations in the quasi-static fields and are accelerated in the forward direction by the transversal and longitudinal components of the laser field[2,13].

To confirm the DLA process, in which strongly directed super-ponderomotive electrons are expected, measurements were performed with two magnetic spectrometers (MSs) with static fields of 0.22 T at 0° and +15° to the laser axis and with three approximately 1 T MSs at ±10° and 170° (Figure 1(a)). BASF-MS and tritium type (TR) imaging plates (IPs) were used as detectors to register electrons and protons accordingly.

The energy dispersion was simulated for each MS using a 2D magnetic field distribution measured at the height of the entrance slit. In the case of the 1 T MS, the field distribution between two magnets is very flat with strong gradients near the spectrometer walls. The experimental error in the energy measurements does not exceed 2% and is mainly caused by the 300 µm size of the entrance slit. This allows a reliable measurement of electron spectra from 1.5 to 100 MeV.

https://doi.org/10.1017/hpl.2024.85 Published online by Cambridge University Press

The magnetic field distribution in the 0.22 T MS was less flat and the energy resolution above 10 MeV was 10 times worse than in the case of the 1 T MS, also due to an entrance hole with a diameter of 1 mm.

The 1 T MSs were equipped with extension sections for measuring high-energy ions and protons up to 100 MeV. In order to filter out carbon and oxygen ions from the signal generated by ions and protons, two superimposed IP layers were used, with the first serving as a filter. The calibration curves for the BASF-MS IP in the case of electrons and the TR-IP in the case of protons were taken from Ref. [41] and used to evaluate the electron and proton energy distributions.

The angular distribution of the electron beam was measured by means of a stack of three stainless steel cylindrical plates of 3 mm thickness each. The cylinder stack had a curvature radius of 300 mm and was placed 300 mm away from the target position (Figure 1(a)). The observation angle was $\pm 12^\circ$ in the horizontal and vertical directions. A horizontal, 4 mm wide slit centred at the height of the laser pulse allowed the electrons to propagate to the MSs, which were positioned 40 cm from the target behind the cylinder stack. In order to map the position of the electron beam in space, small holes with a 20 mm interval in the vertical and horizontal directions were drilled into the front plate. Large-area IPs were placed between the first and the second, and the second and the third, cylindrical plates to map the spatial distribution of electrons with $E > 3.5$ MeV and $E > 7.5$ MeV, respectively.

3. Experimental results of electron and proton acceleration from foams

As mentioned above, the ns pulse, which preceded the relativistic sub-ps pulse, was sent to the foam layer to convert it into an NCD plasma. After 3–5 ns delay, the sub-ps relativistic pulse interacted with plasma and triggered the DLA. Figure 2 shows a ns pulse used to ionize a foam layer (Figure 2(a)), the energy distribution of electrons (Figure 2(b)) and protons (Figure 2(c)) accelerated by the PHELIX sub-ps pulse and an angular distribution of electrons with $E > 7.5$ MeV detected using the cylinder stack (Figure 2(d)).

In this shot, a 450 ± 50 μm thick foam layer of 2 mg/cm^3 density was pre-ionized by the ns pulse of 10^{13} W/cm^2 intensity and 3 ns pulse duration. A delay between the ns pulse and the sub-ps relativistic laser pulse, measured from the rising edge of the ns pulse, was 3 ± 0.5 ns. The ns pulse was focused on target by the same focusing parabola as the sub-ps pulse.

The electron spectra were measured at 0°, $\pm 10^\circ$, $+15^\circ$ and $+170^\circ$ to the laser axis. The electron energy distribution was approximated by an exponential function with effective temperatures from 10–11 MeV ($\pm 10^\circ$, 15°) up to 15 MeV (0°), which is 10 times higher than the ponderomotive potential. In the angular distribution of electrons of more than 7.5 MeV, we observed a shift of the DLA beam by $2.5^\circ \pm 0.5^\circ$ from the laser axis (Figure 2(d)). The half-angle at the FWHM of the IP image, caused by DLA electrons with $E > 7.5$ MeV, is $13^\circ \pm 1.5^\circ$.

Examining the proton spectra (Figure 2(c)), we observe typical target normal sheath acceleration (TNSA) features at $\pm 10^\circ$ characterized by an exponential decrease in proton number with increasing energy and a cut-off at approximately 16 MeV. Even at $+170^\circ$ the proton spectrum has a cut-off, but with four times lower energy than in the forward direction.

In other shots, the parameters of the foam and ns pulse were as follows: 3×10^{14} W/cm^2 intensity, 1.5 ns pulse duration, 4.5 ± 0.5 ns delay between the ns and sub-ps pulses and the 2 mg/cm^3 CHO foam was 450 ± 50 μm thick. The measured electron and proton spectra typical for these conditions are shown in Figures 3(b) and 3(c), and the electron angular distribution is shown in Figure 3(d).

The well-collimated electron beam propagates along the laser at a half-angle of 7°, half the size shown in Figure 2. The MSs, which were arranged at $\pm 10^\circ$ to the laser axis, show a partially non-Maxwellian electron energy distribution with a maximum energy of 60–70 MeV, which is achieved at a detection level of 10^8 electrons/(MeV sr). The strong dependence of the DLA on the angle to the laser axis (see, e.g., Ref. [13]) suggests that these energies are far below those in the centre of the DLA cone shown in Figure 3(d).

The proton spectra with the maximum measured energy of 2–4 MeV shown in Figure 3(c) are not typical for TNSA as the cut-off energy is not present. In addition, we observed damage to the radiochromic film (RCF) layers in the RCF stack located 8 cm from the target position caused by the laser emerging from the plasma (Figure 3(e)). This means that the laser energy was not completely absorbed in the plasma as in the case shown in Figure 2. All of this, together with the low divergence of the electron beam, can be explained by the strong 2D expansion of the front and rear foam sides and the essential reduction of the plasma mass density on the laser axis at higher intensity of the ns pulse and longer ns delay (see also Figure 5(c) in the next section).

The different features of the proton and electron spectra in Figures 2 and 3 show the importance of a detailed study of the time-dependent properties of foam layers heated by ns pulses, using a 2D HD code that takes into account the specific foam structure and the high aspect ratio (ratio of foam thickness to laser focal spot) of the interaction.

4. Two-dimensional hydrodynamic simulations of the interaction of the nanosecond pulse with low-density porous matter

The main physical phenomenon accompanying plasma formation in low-density foams under the action of ns laser pulses is the process of pore homogenization, which

https://doi.org/10.1017/hpl.2024.85 Published online by Cambridge University Press

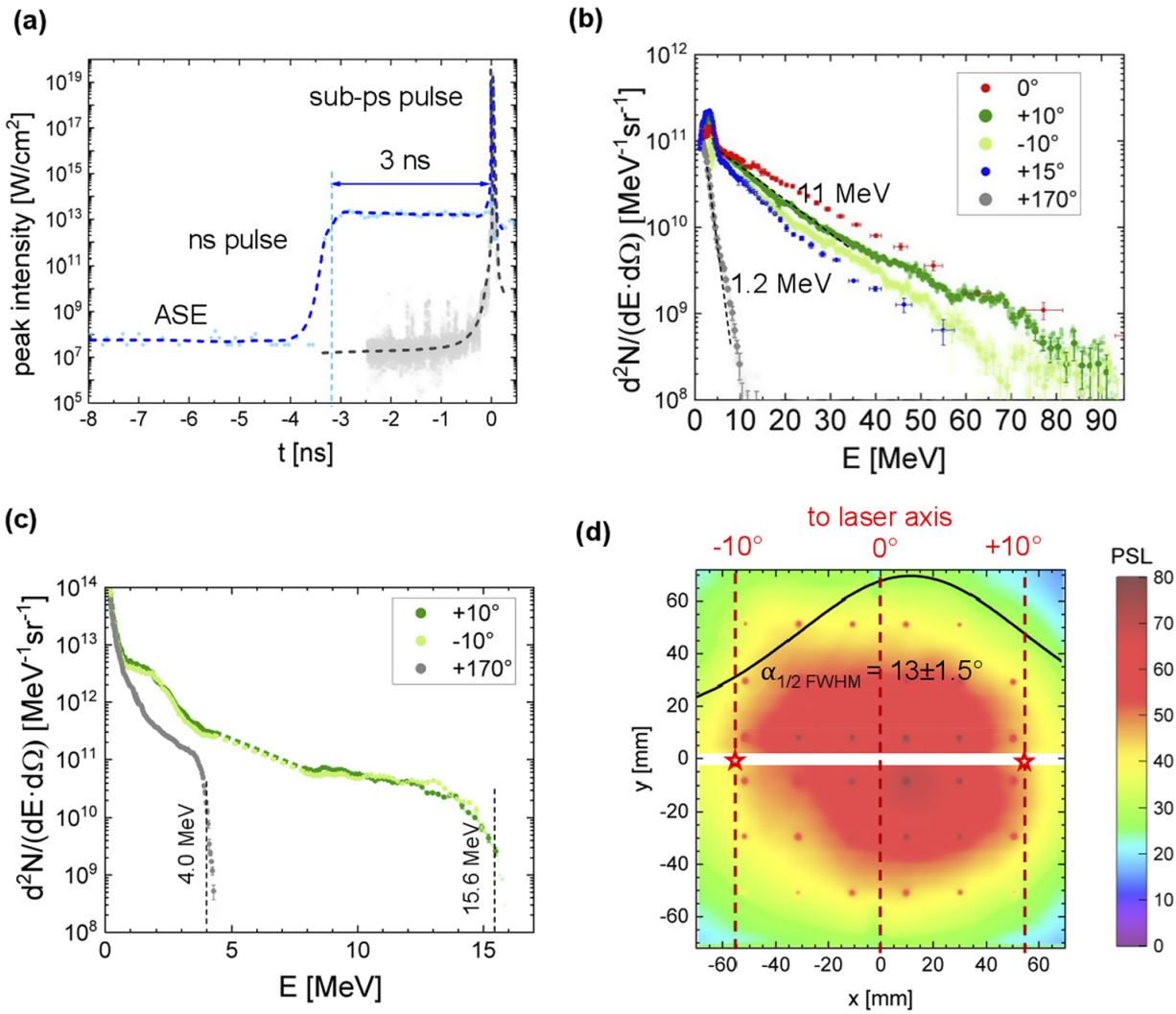

Figure 2. (a) Nanosecond pulse of 10^{13} W/cm^2 intensity and 3 ns duration used to ionize a 450 ± 50 μm thick polymer foam layer of 2 mg/cm^3 density. (b) Energy distribution of electrons and (c) protons accelerated by the PHELIX sub-ps pulse. (d) Angular distribution of electrons with $E_e > 7.5$ MeV detected using the cylinder stack. In this shot, the delay between the ns pulse and sub-ps relativistic laser pulse was 3 ± 0.5 ns. The positions of the magnetic spectrometers are marked with red stars.

equalizes the mass density in the process of ion–ion collisions of the plasma flows inside the pores[39].

In the partially homogenized plasma, the fraction of internal energy is contained in the energy of the turbulent motion of plasma flows inside the pores. This is the reason why during the period of homogenization the directed HD motion and energy transfer by electron conductivity in such a plasma are largely suppressed[26–30,39,42,43]. The duration of homogenization depends on the parameters of the porous structure and the power of the heating source, in our case laser radiation.

In this work, 2D axially symmetric numerical calculations of a laser heating wave in a micro-sized porous CHO substance were performed using the NUTCY-F program[44], which accounts for the laser radiation absorption as well as the 2D HD and thermal energy transfer in partially homogenized plasma, according to the models, which is presented in detail in Refs. [42,43].

The determining factor for the calculation of the interaction of laser radiation with a porous substance and the properties of the resulting plasma in numerical codes is the time-dependent degree of homogenization (density equalization) of the latter. The degree of homogenization is calculated as a result of ion–ion collisions in the plasma flows of matter inside the pore[42]:

$$H(x,t) \equiv \frac{m_h}{m_0} = 1 - \left[1 - 2\int_0^t \frac{dt'}{\tau(x,t')}\right]^{1/2}. \qquad (1)$$

In this expression, m_h and m_0 are, respectively, the mass of the pore homogenized up to the moment t and the total mass of the pore; τ is the time of complete homogenization of the individual pore due to diffusion broadening of dense elements of the medium (initially, the pore walls) in the process of ion–ion collisions of plasma flows inside the pores[39,42].

https://doi.org/10.1017/hpl.2024.85 Published online by Cambridge University Press

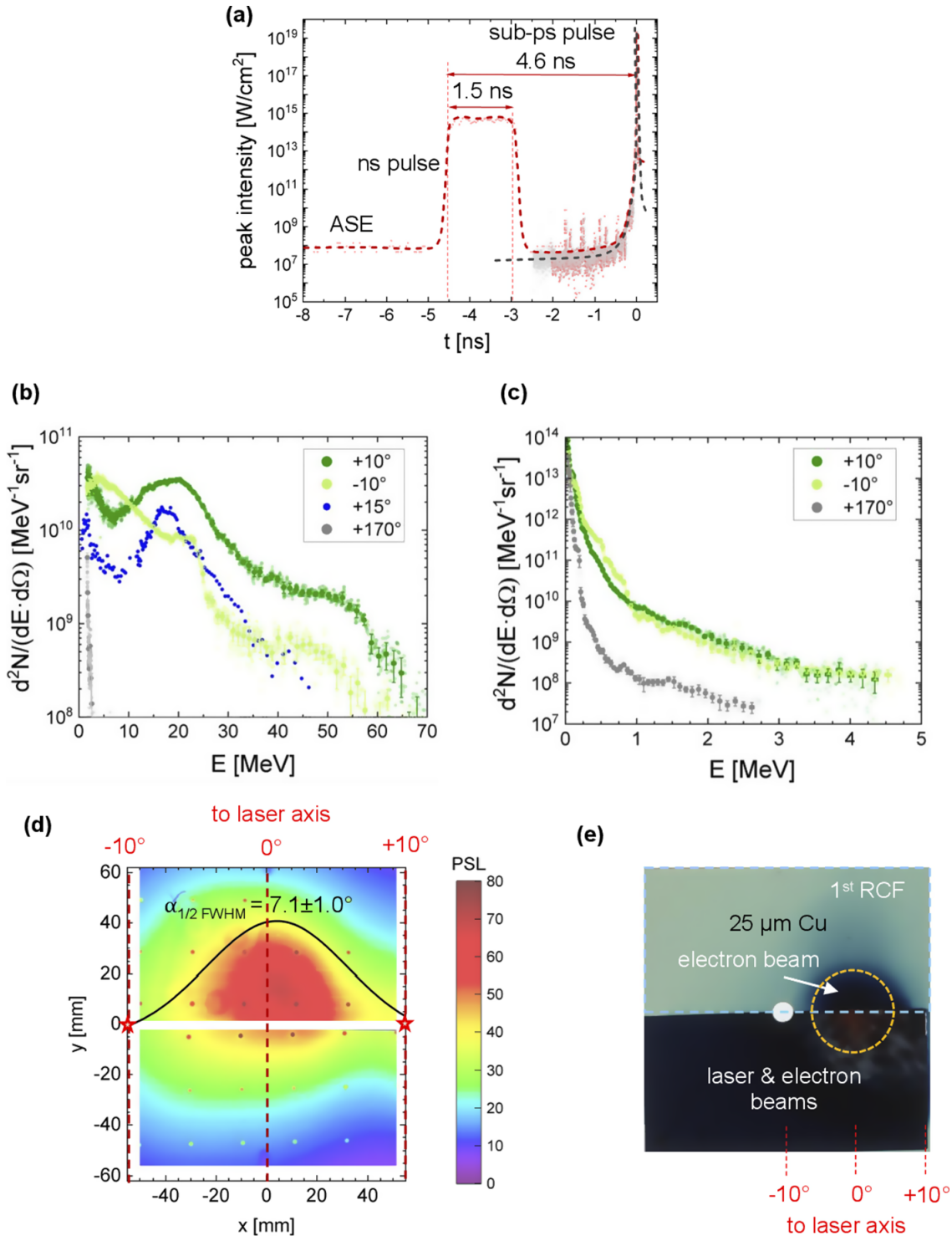

Figure 3. (a) Nanosecond pulse of 3×10^{14} W/cm^2 intensity and 1.5 ns duration used to ionize a 450 ± 50 μm thick polymer foam layer of 2 mg/cm^3 density. (b) Energy distribution of electrons and (c) protons accelerated by the PHELIX sub-ps pulse. (d) Angular distribution of electrons with $E > 7.5$ MeV detected using the cylinder stack; here the positions of the magnetic spectrometers are marked with red stars. (e) RCF stack, half covered with a Cu foil, hit by the laser pulse and DLA electrons. In this shot, the delay between the ns pulse and the relativistic sub-ps laser pulse was 4.5 ± 0.5 ns.

The time of complete homogenization of the individual pore can be expressed as follows:

$$\tau = \frac{\delta_0^2}{V_i^2 \tau_{ii}} \approx 2.4\times10^{-11}\frac{Z^4\delta_0^2\rho}{A^{1/2}T^{5/2}}, \qquad (2)$$

where V_i is the ion velocity of colliding plasma flows, τ_{ii} is the time of ion–ion collisions, T is the temperature of the heated pore's walls in keV, ρ is the average density of the porous substance in g/cm^3, δ_0 is the average pore size in μm and Z is the mean ion charge.

https://doi.org/10.1017/hpl.2024.85 Published online by Cambridge University Press

The absorption coefficient of laser radiation is calculated in accordance with the degree of homogenization as the sum of the inverse bremsstrahlung absorption coefficient for the homogenized part of the plasma with a weight factor H and the inverse value of geometric transparency length of the non-homogenized part of the plasma with a weight factor $1 - H$[42]. The geometric transparency length is calculated as follows[39]:

$$L \approx 5 \times 10^{-4} \times \left(\frac{\rho_s}{\rho}\right)^{1-\alpha} \delta_0, \quad (3)$$

where ρ_s is the density of the pore wall material; α is the fractal parameter, which is equal to 0.8 for micro-size porous substances having, as a rule, a mixed membrane–filament structure.

The properties of partly homogenized laser-produced plasma are described under the assumption that the non-homogenized part of the plasma does not contribute to pressure or electron thermal conductivity. The pressure P_{ph} and thermal diffusion coefficient χ_{ph} are calculated from the corresponding values of the fully homogenized plasma as $P_{ph} = H \cdot P_h$ and $\chi_{ph} = H \cdot \chi_h$[43]. In the calculations of low-density plasmas in the present work, the equation of state of the homogenized part of the plasma is assumed to be as an ideal gas. The parameters of the calculated porous substance were chosen as follows: the average density – $\rho = 2$ mg/cm^3; the density of pore wall – $\rho_s = 1$ g/cm^3; the average pore size – $\delta_0 = 1$ μm. The average thickness of the pore wall is calculated as $b_0 = 6.93 \times 10^{-3}$ μm for fractal parameter $\alpha = 0.8$ in accordance with the following relation[39]:

$$b_0 = \left(\frac{\rho}{\rho_s}\right)^{\alpha} \cdot \delta_0. \quad (4)$$

2D numerical simulations by the NUTSY-F code were carried out for two cases of ns pulses used in the PHELIX experiment. The intensity of the ns pulse and the delay between the relativistic ns and sub-ps laser pulses determine the speed of the ionization wave and the time of structure homogenization and finally the difference in the density profiles.

The first case (Figure 2(a)) is the pulse with intensity of 1.2×10^{13} W/cm^2 and duration of 3 ns, while the second one (Figure 3(a)) is the pulse with intensity of 3×10^{14} W/cm^2 and duration of 1.5 ns with the continuation of the calculation after the end of the pulse until 4.5 ns, when the relativistic pulse interacts with plasma. In both cases, the radius of the laser beam was 6.7 μm and the thickness of the 2 mg/cm^3 foam was 450 μm

The question of pre-heating of the target by thermal plasma radiation in the energy range of soft X-ray photons was investigated in one-dimensional (1D) modelling of the interaction of nanosecond laser pulses with a layer of continuous matter under PHELIX irradiation conditions using the radiation HD code RADIAN[45]. This is an important issue because the homogenization time strongly depends on the temperature and the mean ion charge Z, as follows from Equation (2). It was found that despite the fact that the plasma self-radiation contains an insignificant fraction of the absorbed laser energy of about 4%–5%, the radiative energy transfer leads to a pre-heating of the target up to 5–7 eV. The temperature of 7 eV and the corresponding degree of ionization 1.8 of the porous substance were selected as initial values.

Figures 4(a)–4(d) show results of numerical simulations using the 2D NUTCY-F code made for a 2 mg/cm^3 450 μm thick CHO foam layer and ns pulse of 1.2×10^{13} W/cm^2 intensity and 3 ns duration used in the experiment. In all figures, the grey area corresponds to the initial position of the 450 μm thick foam layer. The 2D mass density distribution is shown in Figures 4(a) and 4(c) for 1 and 3 ns after the onset of the ns pulse.

During the propagation of the laser pulse, the plasma is partially blown out of the interaction region, which is shown by the blue–green region representing the under-dense plasma. Here, the r-axis shows the foam density distribution in the radial direction, and the z-axis shows the foam density distribution along the axis of the laser pulse. The red region denotes a wave propagating inside the foam in the radial direction and having a mass density about twice the initial one; the yellow region represents a region not perturbed by the ns pulse, with an initial foam mass density of 2 mg/cm^3.

Figures 4(b) and 4(d) show profiles of the mass density (black line), electron density (blue line) and temperature (red line) along the z-axis (laser axis) established up to the moment of the interaction with the relativistic pulse.

The profiles in Figures 4(b) and 4(d) consist of the low-density region corresponding to the plasma expanded towards the laser pulse, the shock region and the NCD part. With time, the characteristic scale of the plasma up-ramp towards the laser increases, while the thickness of the NCD part decreases.

The propagation of a 2D energy transfer wave in a porous substance is regulated by the contributions of the laser absorption wave in the longitudinal direction (along the laser beam) and the HD wave of energy transfer in the transverse direction. In continuous matter of subcritical density, the front of the laser heating wave is located at the depth of the area where absorption of the laser energy due to the inverse bremsstrahlung occurs[46]. In a porous substance, the propagation of a longitudinal laser absorption wave can be limited by the speed of the homogenization wave[27].

NUTCY-F simulations show that during exposure to the laser pulse, a 2D hydrothermal energy transfer wave propagates in a porous substance with an average speed of 9×10^6 cm/s in the longitudinal direction. The characteristic

https://doi.org/10.1017/hpl.2024.85 Published online by Cambridge University Press

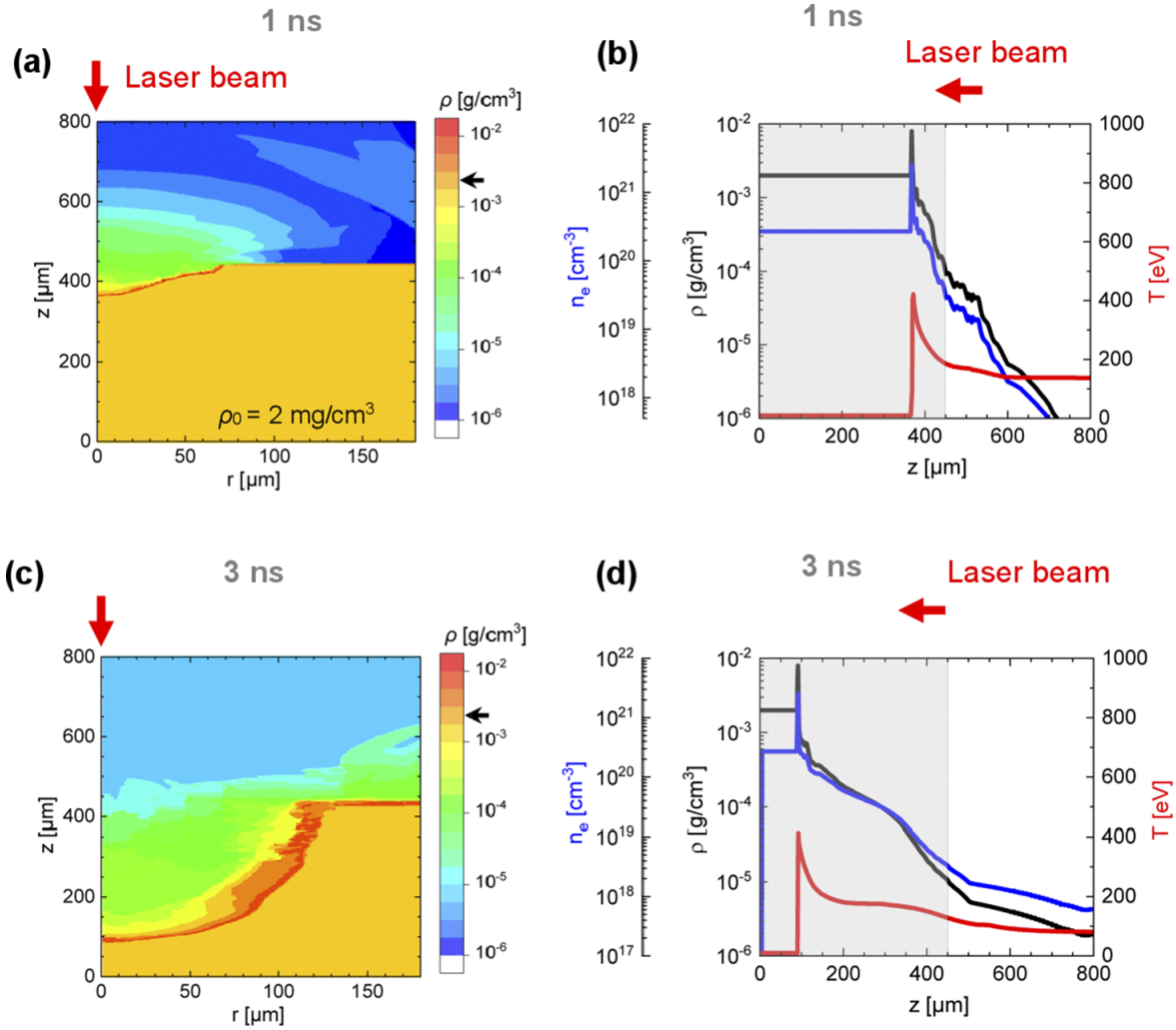

Figure 4. (a), (c) 2D map of the mass density (g/cm^3) at 1 and 3 ns after the interaction of the laser pulse of 10^{13} W/cm^2 with the structured foam, where z is the cylindrical axis of symmetry and r is the radial axis, both given in μm. The initial foam size is 450 μm in the z-direction and 180 μm in the r-direction. The initial foam density of 2 mg/cm^3 is shown with a black arrow on the colour bar. (b), (d) Plasma density and temperature profiles at the time of the relativistic pulse arrival: mass density (black line), electron density in cm^{-3} (blue line), and electron temperature in eV (red line), along the laser propagation direction z. The grey shadow shows the initial position and density of the foam.

temperature near the wave front is about 0.5 keV and the pore homogenization time is 24 ps. As a result, during 3 ns of the laser pulse duration, only a part of the layer with a thickness of about 350 μm is involved in the interaction. In the transverse (radial) direction, the wave propagates a distance of 120 μm in 3 ns, which is 18 times the radius of the laser beam. This gives an estimate of the average radial velocity of 4×10^6 cm/s. Due to the radial plasma expansion, the areal density of the plasma along the laser axis decreases with time and is 80% of the initial value at $t = 1$ ns, 50% at $t = 2$ ns and 30% at $t = 3$ ns.

To establish the role of the 2D effect, 1D simulations were performed using the HD code DIANA-F[43] for the same conditions of the ns pulse that were used in the 2D NUTSY-F version (Figure 2(a)). In addition, the DIANA-F code uses the same algorithms of calculation of the laser absorption coefficient, equation of state of matter and coefficient of thermal conductivity in a partly homogenized plasma as the NUTSY-F. The 1D modelling of the ns pulse interaction with layers of porous matter of 2 mg/cm^3 density showed a weak dependence of the results on the initial density of solid elements in the range of 0.1–1 g/cm^3 and the type of structure (open or closed pores).

The 1D heat wave passes the 450 μm thickness of the layer during the time of approximately 1 ns with a velocity of 4.4×10^7 cm/s, five times faster than in the 2D case. The characteristic temperature near the wave front is about 1 keV and the time of pore homogenization is 2 ps. The lower 2D wave speed arises from the redistribution of energy due to the transverse movement of the matter, which leads to a lower temperature (0.4 keV instead of 1 keV in the 1D case). The decrease in temperature leads to a significant increase in the homogenization time due to its $T^{-5/2}$ dependence on temperature. Furthermore, the decrease in wave speed is

https://doi.org/10.1017/hpl.2024.85 Published online by Cambridge University Press

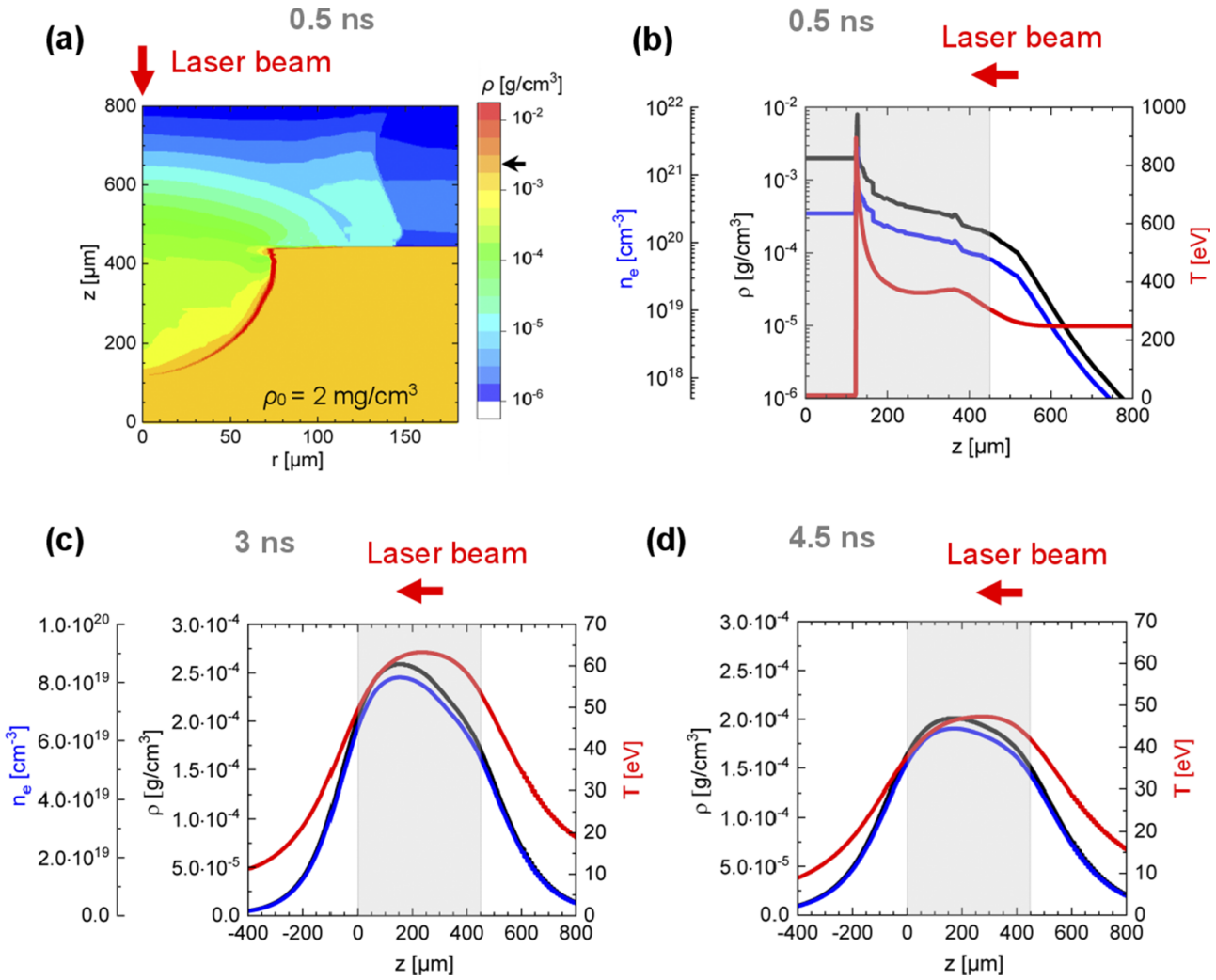

Figure 5. (a) Two-dimensional mass density profile at 0.5, 3 and 4.5 ns during and after interaction of the 3×10^{14} W/cm^2 ns pulse of 1.5 ns duration with the structured foam. Here, z is a cylindrical symmetry axis and the direction of laser pulse propagation, while the r-axis corresponds to the radius of the foam disc considered in the simulations (x, r in μm). (b)–(d) Plasma density and temperature profiles along the z-axis at 0.5, 3 and 4.5 ns: mass density in g/cm^3 (black solid line), electron density in cm^{-3} (blue solid line) and electron temperature in eV (red solid line).

much greater due to the 12 times longer homogenization time than due to the redistribution of energy for the transverse motion.

Figure 5 shows the results of NUTCY-F simulations performed for the ns pulse of 3×10^{14} W/cm^2 intensity and 1.5 ns duration (Figure 3(a)). A 2D distribution of the plasma mass density at 0.5 ns after foam irradiation is shown in Figure 5(a), while Figures 5(b)–5(d) show the distributions of mass density, electron density and temperature along z-axis at 0.5, 3 and 4.5 ns after the start of the ns pulse. As soon as the shock wave reaches the back of the foam ($\geq$1 ns), plasma starts to expand in both directions and the overall plasma density decreases rapidly. At 3 ns it reaches a peak value at $0.09n_{cr}$ (Figure 5(c)) and at 4.5 ns at $0.06n_{cr}$ with $0.03n_{cr}$ at FWHM of the plasma profile (Figure 5(d)). The expansion of the rear part of the foam is indirectly confirmed by the measurement of the low-energy proton spectrum without cut-off (Figure 3(c)), which would be expected in the case of a sharp density gradient (TNSA).

Due to strong 2D expansion, at the moment of the sub-ps pulse arrival after 4.5 ns, the areal density of the plasma target at the laser axis drops 40 times compared to the initial one, so that the energy of the relativistic pulse is not completely absorbed in the plasma. In the experiment, this is confirmed by damage to the RCF stack located at a distance of 8 cm from the target (Figures 3(b) and 3(e)) by the relativistic laser pulse.

If a laser pulse with a higher intensity of 3×10^{14} W/cm^2 and a duration of 1.5 ns irradiates the foam with the same density of 2 mg/cm^3 and a thickness of 450 μm, the energy transfer wave velocity is significantly higher than in the case discussed in Figure 4. This is due to an increase in temperature and associated shortening of the duration of homogenization. The velocity of the hydrothermal wave in

https://doi.org/10.1017/hpl.2024.85 Published online by Cambridge University Press

the 2D NUTCY-F simulation of the porous substance is 8×10^7 cm/s with a homogenization time of a single pore of about 5 ps.

Such a wave propagates through a 450 μm thick layer of porous matter in a time of about 0.55 ns. After this, re-refraction waves propagate inside the layer of homogenized substance towards each other, both from the irradiation surface of the layer and from its rear surface. By the time of 4–5 ns, this leads to a quasi-symmetric density distribution along the direction of incidence of the laser beam, since the delay in the onset of propagation of the unloading wave from the rear surface at this moment is only 10%. In the transverse direction, the wave propagates in 1 ns up to a distance of approximately 80 μm, which is more than an order of magnitude larger than the radius of the laser beam.

Please note the presence of super-critical peaks in the electron density, which can be seen in Figures 4 and 5. These peaks are related to the effect of the shock wave behind the front of the laser absorption wave in a subcritical plasma. Over time, the shock wave front catches up with the front of the laser absorption wave. This effect in the subcritical plasma of a continuous and porous substance was investigated in Ref. [47].

The 1D DIANA-F simulation leads to a wave velocity of 4×10^8 cm/s with a homogenization time of 0.4 ps for a single pore, which is a factor of five higher than in the 2D NUTCY-F case. In the case of the 1D approach for a continuous medium, the velocity of the hydrothermal wave would be overestimated by a factor of 10 compared to the 2D result for porous medium.

The role of laser absorption and homogenization waves in the energy transfer is discussed in Ref. [44] as a function of the foam and laser parameters. There it is also shown that the 2D effect becomes greater with increasing density ρ and geometrical aspect ratio (foam thickness-to-laser beam radius ratio) and with decreasing laser intensity I. In addition, in the case of the laser absorption wave, the 2D effect increases with increasing laser wavelength and wave passage time. In the case of the homogenization wave, the 2D effect increases with increasing pore size.

Further, the role of a ps pre-pulse of the PHELIX pulse in the additional plasma heating and homogenization was investigated for the case of a ns pulse with an intensity of 1.2×10^{13} W/cm^2, when the foam of about 100 μm remains undisturbed by the ns pulse. The plasma formed at the end of such a nanosecond pulse (Figures 4(c) and 4(d)) was affected by a PHELIX picosecond pre-pulse with an intensity that increases from the high contrast level of the ns-ASE at 10^8–10^9 up to 5×10^{13} W/cm^2 during the first 70 ps and to 5×10^{15} W/cm^2 in the next 20–25 ps. Part of the foam layer with a thickness of 100 μm and an initial density of 2 mg/cm^3 is pre-heated by self-irradiation of the plasma up to at least 10 eV and is not fully ionized and homogenized. During the short interaction time, the density distribution remains practically unchanged and 2D effects play an insignificant role.

In the homogenized under-dense part of the plasma target generated by the ns pulse, the velocity of the energy transfer wave is determined by the laser absorption wave velocity of about 4×10^8 cm/s in the pre-pulse phase with an intensity of 5×10^{13} W/cm^2 and 8×10^9 cm/s in the pre-pulse phase with an intensity of 5×10^{15} W/cm^2. The energy transfer wave caused by the ps pre-pulse therefore needs about 70 ps to cross 350 μm of the homogenized part of the layer.

Due to the increase of the plasma temperature at the front of the heating wave up to 1 keV in the second pre-pulse phase with an intensity of 5×10^{15} W/cm^2 and the corresponding reduction of the homogenization time to 4 ps according to Equation (2), the homogenization wave penetrates into the non-homogenized part of the layer with an average speed of 8.7×10^8 cm/s and passes through 100 μm in about 12 ps. In this way, the rest of the foam is transformed into a homogeneous NCD plasma with an electron density of $0.65 n_{cr}$.

This shows the important role of the ps pre-pulse, which should be sufficiently intense and long for the homogenization of the NCD part, as otherwise DLA only takes place in the density up-ramp.

5. Three-dimensional particle-in-cell simulations of direct laser acceleration of electrons in plasma

The simulations of the DLA process in NCD plasma were carried out by means of the Virtual Laser Plasma Laboratory (VLPL) 3D PIC code[48] for the PHELIX laser parameters described in Section 2. To simulate the measured energy spectra and angular distribution of the accelerated electrons shown in Figure 2, the following data were used: the FWHM duration of the Gaussian laser pulse is 0.7 ps, the elliptical focal spot has FWHM diameters of 16.2 and 14.7 μm and laser energy $E_{FWHM} = 17.4$ J. This results in a laser intensity of 1.72×10^{19} W/cm^2 with a corresponding dimensionless laser pulse field amplitude $a_0 = 3.55$, where $a_0 = eE_y/(mc\omega)$, E_y is the electric field amplitude of the laser pulse, ω is its frequency and m and e are the mass of electron at rest and its charge (scaled as $a_0^2 = 0.73 \times I_{L,18} \times \lambda^2$ with the laser intensity $I_{L,18}$ normalized to 10^{18} W/cm^2 and the laser wavelength $\lambda = 1$ μm).

The plasma was represented by electrons and fully ionized ions of carbon, hydrogen and oxygen, which corresponds to the chemical composition of the polymer foam; see, for example, Refs. [12,21]. The size of the simulation box was 500 μm × 80 μm × 80 μm with boundary conditions absorbing particles and fields in each direction. The size of the numerical cells was 0.1 μm in the x direction (laser propagation) and 0.5 μm in the y and z directions, where y is the polarization direction, and contained four electrons and one ion in each cell.

https://doi.org/10.1017/hpl.2024.85 Published online by Cambridge University Press

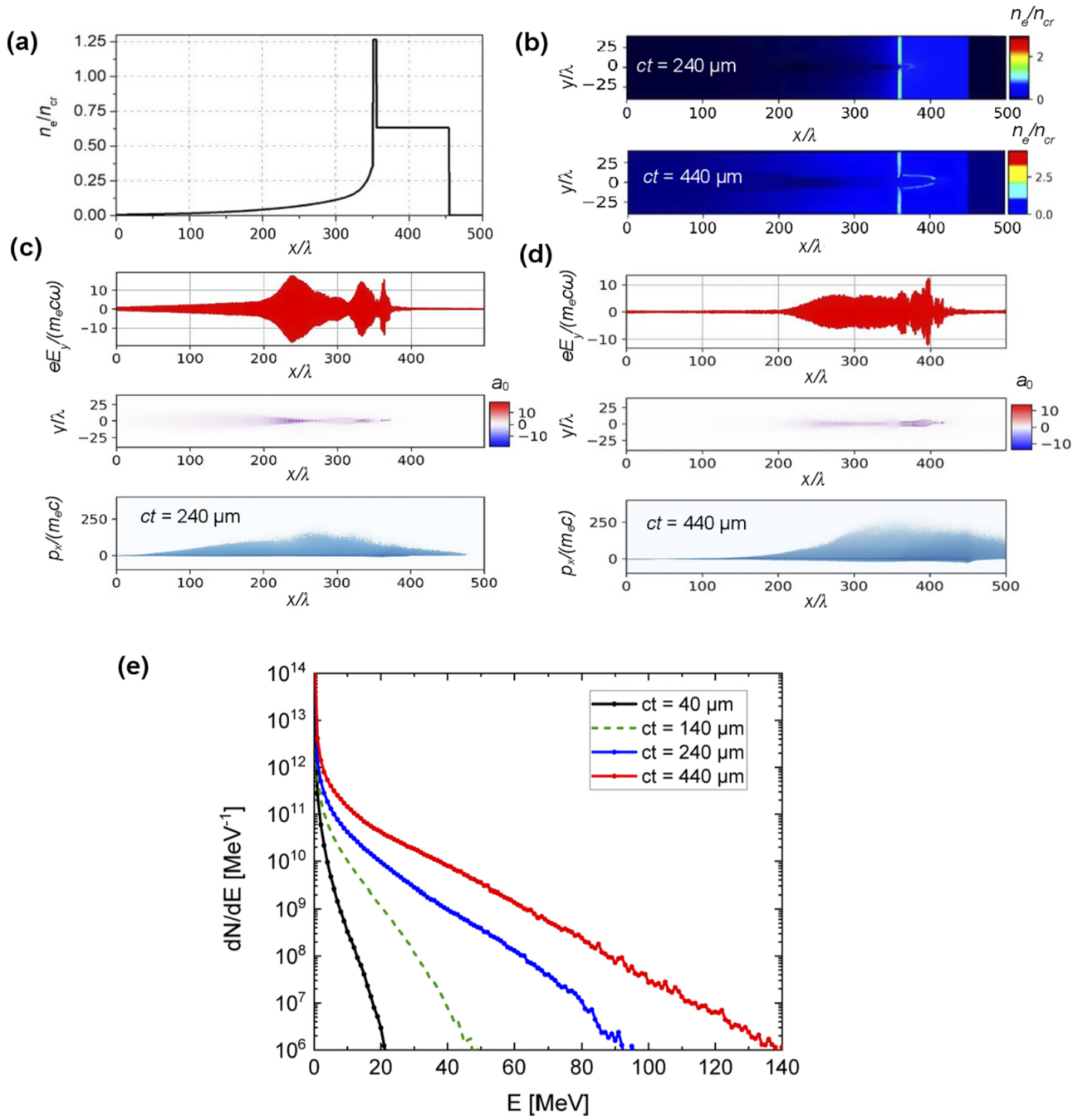

Figure 6. (a) Electron density profile 3.1 ns after action of the ns pulse and ps pre-pulse. (b) Electron density distribution in the *OXY* (laser polarization) plane at $ct = 240$ μm and $ct = 440$ μm. Normalized laser field E_y on the *OX* axis and in the *OXY* plane, as well as the snapshots of the electron distribution in the phase plane (x, p_x) at (c) $ct = 240$ μm and (d) $ct = 440$ μm. (e) Energy distribution of electrons inside the simulation box at $ct = 40$, 140, 240 and 440 μm.

In the PIC simulations, the initial electron density distribution along the laser pulse axis (Figure 6(a)) corresponds to the mass density profile (black curve in Figure 4(d)) in case of fully ionized CHO plasma with $Z = 4.2$. The density profile of the expanded plasma with the electron density $n_e/n_{cr} = 0.01$ at $x/\lambda = 0$ was approximated by a sum of two exponents with a characteristic plasma scale length of 100 μm for the low-density part and with a plasma scale length of 10 μm for the sharp density increase near the shock.

The NCD part of the plasma of approximately 100 μm length corresponds to a foam region with an initial mass density of 2 mg/cm^3 (1.54×10^{20} atoms/cm^3) and a corresponding electron density of $0.65n_{cr}$, which is unperturbed by the ns pulse.

Figure 6(b) shows the electron density distribution in the relativistic plasma channel in the *OXY* laser polarization plane at $ct = 240$ μm and $ct = 440$ μm (time $t = 0$ corresponds to the maximum laser pulse intensity on the

https://doi.org/10.1017/hpl.2024.85 Published online by Cambridge University Press

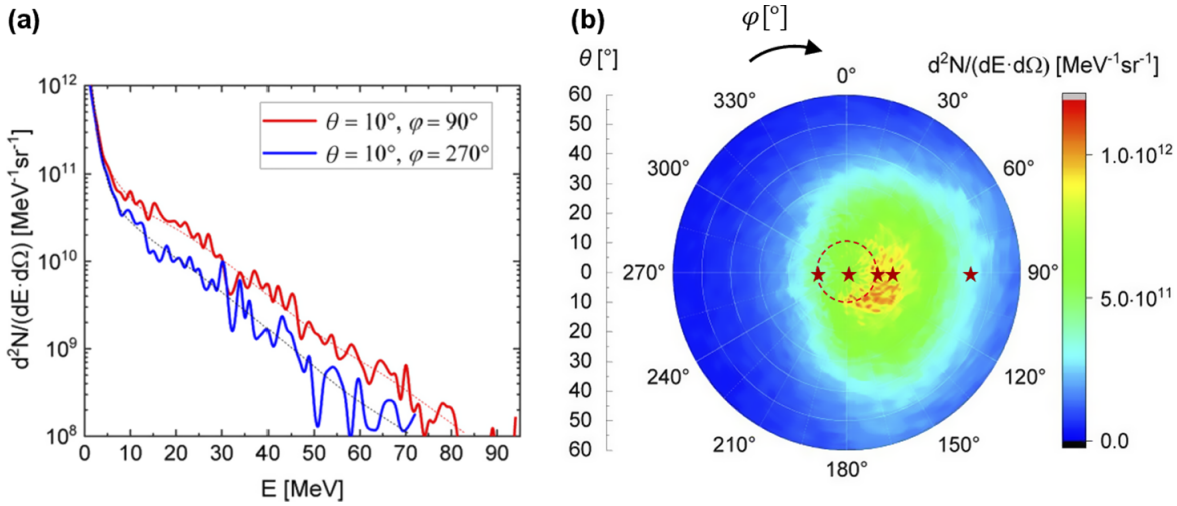

Figure 7. (a) Simulated electron energy distribution per MeV per sr at ±10° to the laser axis ($\theta = 10°, \varphi = 90°$ and 270°). (b) Angular distribution of the electrons with $E > 7.5$ MeV in spherical coordinates with a polar axis OX along the laser propagation direction: $\theta = \arctan\left(\sqrt{p_y^2 + p_z^2}/p_x\right)$, $\varphi = \arctan\left(p_z/p_y\right)$.

target front side, $x/\lambda = 0$). Figures 6(c) and 6(d) present the normalized laser field E_y on the OX axis and in the OXY plane, as well as snapshots of the electron distribution in the phase plane (x, p_x) at $ct = 240$ μm and $ct = 440$ μm. The energy distributions of electrons inside the simulation box at $ct = 40$, 140m, 240 and 440 μm are shown in Figure 6(e).

If the laser power exceeds the critical value $P_{cr} \approx 17\left(\omega/\omega_p\right)^2$ (in GW)[49], where ω and ω_p are the laser and plasma frequency, respectively, and the laser pulse undergoes relativistic self-focusing and can channel in the plasma. As the power of the PHELIX laser pulse of 100–200 TW is much higher than the critical power for laser self-focusing, the pulse begins to yield filament when it enters the plasma with electron density of greater than or equal to $10^{-3}n_{cr}$. After passing through the unstable filamentation stage, in which each laser filament carries a strong electron current, they merge into a single channel[2,50]. This happens since the co-directed currents in the laser filaments can attract each other magnetically, forming a super-channel (magnetic self-focusing[2]). Figures 6(b)–6(d) show a single channel formed in the plasma for $ct = 240$ and 440 μm. The observation of a super-channel of approximately 5 μm in diameter by propagation of a 10 TW VULCAN laser pulse in performed plasma with density of more than 2×10^{19} cm^{-3} was reported in Ref. [51]. The same channel size was obtained in 3D PIC simulations performed for the PHELIX parameters and an NCD plasma slab[13,33].

During its interaction with plasma prepared by the ns pulse, the PHELIX pulse propagates first through the under-dense part with exponentially increasing electron density and reaches a steep part of the density gradient with a characteristic plasma scale length of 10 μm in front of the shock followed by the NCD part. The head of the 200 μm long pulse passes through the over-dense shock-front and enters the NCD part ($n_e/n_{cr} = 0.65$) at $ct = 240$ μm (Figure 6(c)). At this time, the distribution of the normalized laser field along the laser pulse axis is rather pulsating in space, reaching at some points $a_0 \simeq 15$ and on average approximately equal to 10, three times higher than those in vacuum (Figure 6(c)). At a later time corresponding to $ct = 440$ μm, where the substantial part of the laser pulse propagates in NCD plasma with an initial mass density of 2 mg/cm^3, the laser field distribution stabilizes at average $a \simeq 7$. Simulations show that the DLA is most intense between $ct = 240$ and 440 μm, where electrons gain a momentum of $p_x \simeq 50m_ec$–$250m_ec$.

This trend can be seen even more clearly in Figure 6(e), which shows the dynamics of the DLA process within the simulation box. The electron energy increases continuously from $ct = 40$ μm (under-critical plasma) to $ct = 440$ μm (NCD). At $ct = 240$ μm, the maximum energy reaches 90 MeV and increases further to 140 MeV up to $ct = 440$ μm, where most of the electrons are accelerated in front of the shock in the very steep density up-ramp and in the NCD part.

In the PIC simulations, the electrons leaving the plasma were recorded at an angle $\theta = 10°$ to the laser axis in a plane perpendicular to the laser polarization, $\varphi = 90°$ and 270°, as in the experiment. Figure 7(a) shows the electron energy spectra leaving the plasma in these directions. The electron energy distribution was approximated by a Maxwellian function with an effective temperature of 11 MeV for electron energies of more than 6 MeV, which is in good agreement with the measurements (see Figure 2(b)). The angular distribution of the electrons with $E > 7.5$ MeV is shown in Figure 7(b) in spherical coordinates with a polar axis OX along the laser propagation direction: $\theta = \arctan\left(\sqrt{p_y^2 + p_z^2}/p_x\right)$, $\varphi = \arctan\left(p_z/p_y\right)$.

https://doi.org/10.1017/hpl.2024.85 Published online by Cambridge University Press

Here, the positions of the MSs are denoted with red stars, while the red dashed circle shows the measured angular size and position of the DLA beam from Figure 2(d). In simulations, due to the hosing instability at the end of the beam propagation in the plasma channel, the electron beam deviates from the laser axis by 10°, while in the experiment it deviates by only 2.5°. Experimental statistics obtained over more than 300 shots in many experimental campaigns at the PHELIX facility show that the hosing does not exceed 6° in any of the measurements. This is an important aspect for applications such as generation of MeV bremsstrahlung when the foam is stacked with a high-Z converter[13,37,38].

The reason for the discrepancy between the electron beam angular distribution obtained in the experiment and that in the simulations may be the temperature of the background electrons, which was set to zero in these simulations. Simulations made for slightly different PHELIX parameters ($a_0 = 4.0$, focal-spot size 25 μm) show that filamentation and hosing processes occurring at later times are numerically stabilized by considering a temperature of 100 eV for the background electrons. This also leads to the longer interaction path of the laser in plasma.

The big advantage of the 3D PIC code compared to the 2D version is that it enables a fairly reliable prediction of the DLA beam charge. Experimentally, the electron beam charge can be estimated from the spectral distribution of electrons $d^2N/(dE \cdot d\Omega)$ measured at different angles to the laser axis, which is integrated over electron energies above the specified one. It is assumed that the electron beam has a Gaussian profile in the horizontal and vertical directions centred at the maximum of the IP-image profile (Figures 2(d) and 3(e)).

The result of this procedure for the laser shot presented in Figure 2 is shown in Figure 8 by a green line describing the angle-dependent electron fluence with five dots at the corresponding positions of the MSs. The maximum of the Gaussian profile is shifted by 2.5° from the laser axis, as it was measured in the experiment. The estimated beam charge of electrons with $E > 7.5$ MeV propagating within the half-angle of 13° at FWHM reaches 32 ± 4 nC. The blue line shows a simulated angle-dependent electron fluence $dN/d\Omega$ with 63 nC directed electrons with $E > 7.5$ MeV at FWHM. The difference in the electron charge is caused by the broader beam-shape obtained in simulations. In the case of the high-intensity ns pulse (Figure 3), the charge of the directional part of the DLA beam ($E > 7.5$ MeV) obtained from the experimental data is 16 ± 2 nC, which is two times lower than in the previous case.

Figure 9 summarizes the results of 3D PIC simulations and shows the energy spectra of all electrons with $p_x > 0$ leaving the plasma for different cases of the plasma density profile.

The charge and effective temperatures (T_{eff}) of the DLA beams are summarized in Table 1. A relatively small difference can be observed between the spectra of electrons that are accelerated in the step-like profile with $0.65n_{\text{cr}}$

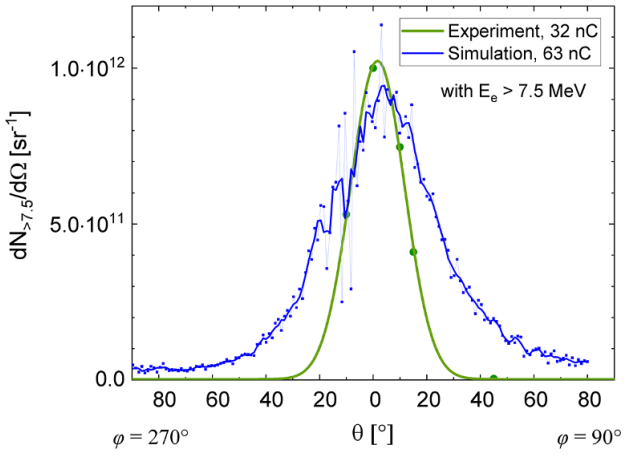

Figure 8. Measured (green line) and simulated (blue line) angle-dependent fluence $dN/d\Omega$ of electrons with energy of more than 7.5 MeV. Green dots denote corresponding positions of MSs in the experiment. The blue curve shows a simulated angle-dependent electron fluence for $E > 7.5$ MeV.

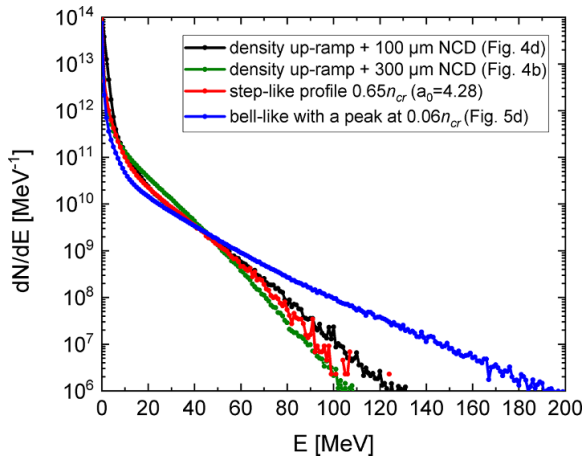

Figure 9. Electron energy spectra simulated for different density profiles: step-like electron density profile with $0.65n_{\text{cr}}$, $a_0 = 4.28$ (red); plasma profiles from Figure 4(b), $a_0 = 3.15$ (green), Figure 4(d), $a_0 = 3.55$ (black) and Figure 5(d), $a_0 = 3.55$ (blue).

(red curve) and the profiles in Figure 4(b) (green curve) and in Figure 4(d) (black curve), which contains a density up-ramp and NCD part. Here, the minor difference occurs at electron energies of more than 40 MeV, where more energetic electrons are generated at the longer plasma up-ramp in case of the profile in Figure 4(d). For correct comparison of the electron spectrum simulated for the step-like profile and $a_0 = 4.28$ (red) taken from Ref. [13] with those obtained, for example, $a_0 = 3.15$ (green), its effective temperature should be reduced by a factor of 1.35 according to the scaling from Refs. [2,50]. This correction results in $T_{\text{eff}} \simeq 7.8$ MeV. Therefore, the electron spectrum from the step-like NCD profile has the lowest effective temperature and the spectrum with the longest up-ramp and the NCD part has the highest one (11 MeV).

Table 1 shows the number of electrons with energies exceeding 7, 40 and 100 MeV for the different plasma density

https://doi.org/10.1017/hpl.2024.85 Published online by Cambridge University Press

Table 1. Number of DLA electrons and their effective temperature for different plasma density profiles.

Plasma density profile/ Spectrum of electrons	Number/Charge of electrons $E > 7$ MeV	Number of electrons $E > 40$ MeV	Number of electrons $E > 100$ MeV	T_{eff} $E > 20$ MeV
Step-like $a_0 = 4.28$[13]/ Red curve, Figure 9	1.1×10^{12} / 176 nC	3.6×10^{10}	-	10.6 MeV
Figure 4(b)/ Green curve, Figure 9	1.6×10^{12} / 256 nC	3.6×10^{10}	-	8.4 MeV
Figure 4(d)/ Black curve, Figure 9	1.4×10^{12} / 224 nC	3.9×10^{10}	1.2×10^{8}	11 MeV
Figure 5(d)/ Blue curve, Figure 9	0.7×10^{12} / 112 nC	5.2×10^{10}	2.0×10^{9}	16.5 MeV

profiles discussed in this work (Figure 9) and the effective electron temperature T_{eff}. Electron beam charges in different energy ranges are determined by electrons escaping the simulation box in the direction of laser pulse propagation. The effective electron temperatures are the results of fitting the spectra obtained in PIC modelling, using the Maxwell distribution for electron energies above 20 MeV.

The total number of electrons with energies above 7 MeV in the black, red and green spectra is very similar and yields (1.1–1.6) $\times10^{12}$ particles. Here, most of the electrons are accelerated in front of the shock in the very steep density up-ramp and in the NCD part (Figure 6(e)).

The blue spectrum in Figure 9 corresponds to the 1 mm long bell-like density profile (Figure 5(d)), with $0.06n_{\text{cr}}$ peak density. It shows the higher effective electron temperatures of 16.5 MeV compared to two times shorter density profiles with the NCD part. According to the 3D PIC simulations, the normalized amplitude of the laser field in the case of expanded under-dense plasma reaches $a_0 = 10$ at $n_e = 0.03n_{\text{cr}}$ and maintains this high value over a long distance. The profile of the ion channel is very straight and does not show a hosing effect. On the descending part of the density profile, the laser field amplitude drops slowly to $a_0 = 5$–6 as the laser pulse approaches the right-hand edge of the simulation box and still carries the rest of the energy. The long acceleration path of the electrons in the presence of a high amplitude of the laser field allows for gaining more energy.

Compared to other profiles, the blue spectrum has the largest number of electrons with energies of more than 40 MeV, but two times less with energies of more than 7 MeV.

6. Discussion

One can optimize the intensity, duration and delay between ns and ps pulses for given laser and foam parameters and desired applications of DLA electrons. Figure 10 shows electron spectra measured along the laser axis in shots on Al-foil and different types of polymer foams. The grey spectrum belongs to the picosecond PHELIX shot with high ns contrast of approximately 10^{-11} at an intensity of 10^{19} W/cm^2 on Al foil, while in the case of the light blue spectrum the foil was pre-ionized with a 3 ns pulse of 10^{14} W/cm^2 intensity. We clearly see an increase of the effective electron temperature, the electron beam charge in

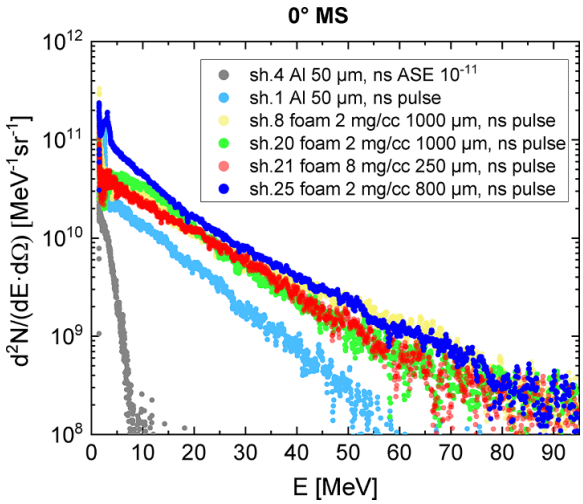

Figure 10. Electron spectra measured at 0° to the laser axis. The grey spectrum belongs to the PHELIX shot with high ns-ASE of approximately 10^{11} at intensity of 10^{19} W/cm^2 on Al foil, while in the case of the light blue spectrum the foil was pre-ionized with a ns pulse. The other colours represent electron spectra measured after irradiation of foams with densities of 2 and 8 mg/cm^3 and thickness between 250 and 1000 µm. All shots were performed with ns pulses in the range of 10^{13}–3×10^{14} W/cm^2 and delay of 3–5 ns between ns and sub-ps pulses.

the direction of the laser axis and the maximum measured energy due to the generation of a pre-plasma.

The other colours show electron spectra measured after irradiation of foams with densities of 2 and 8 mg/cm^3 and thickness between 250 µm and 1000 µm. For all shots performed, ns pulse intensities were between 10^{13} and 3×10^{14} W/cm^2 and the delay was between 3 and 5 ns, which were adjusted to the specific foam parameters.

The energy distribution of the electrons generated in the pre-ionized foams shows very similar overall behaviour in terms of the effective temperature, the maximum detected electron energy and the charge of the DLA beam, confirming once again the stability and robustness of DLA of electrons in pre-ionized foams, which can be used to drive other particle and radiation sources when shot-to-shot stable parameters are required.

The bell-shaped density profile with peak electron densities between $0.1n_{\text{cr}}$ and $0.06n_{\text{cr}}$ shown in Figure 5 can be used to realize a strategy proposed in Ref. [52] for accelerating electrons up to multi-GeV energies with multi-PW laser pulses. It is proposed to start the acceleration at low density to ensure high maximum energy and later

https://doi.org/10.1017/hpl.2024.85 Published online by Cambridge University Press

increase the density to achieve a higher local acceleration rate. By adjusting the density profile, the highest energy can be achieved at the shortest possible distances. Using this strategy, it was numerically proven that energies of over 5 GeV can be reached in such a plasma with a 5 PW laser pulse of 200 fs duration after 1 mm propagation in plasma[52]. Low-density foams offer a good opportunity to create such plasma profiles by adjusting the foam and ns pulse parameters.

In Refs. [53,54], scalings for the temperature and cut-off energy of super-ponderomotive electrons in the laser interaction with a solid target and under-dense plasma are developed based on dozens of PIC simulation results and experimental data. These scalings provide reasonable values for the parameters of the DLA electrons.

Finally, we would like to point out the conditions for the laser focal-spot size and the $f/\#$ number of the focusing parabola used in the PHELIX experiments for successful electron acceleration from sub-mm-long foams. The relatively large $f/5$ number and a focal spot of approximately equal to 15 μm provide a Rayleigh length (R_L) of over 100 μm, which ensures a larger plane laser wave front and softer requirements for the laser focusing. Moreover, the PHELIX focal spot ($\simeq$15 μm) is close to the value required for stable channelling propagation of the laser pulse in plasma[55–57]. A larger focal spot can hinder the formation of a single super-channel if the distances between the filaments are larger than the plasma skin depth[2]. This can lead to stochastic acceleration across the filaments, resulting in a lower effective electron temperature but a larger beam charge than in DLA[57]. In the opposite case, the sharp focusing can lead to strong distortion of the laser wave front in the pre-plasma, which will prevent stable laser propagation. The optimal size of the laser focal spot for effective DLA with multi-PW laser pulses in under-dense plasmas is discussed in Refs. [54,58].

7. Summary

Long-scale low-density polymer foams pre-ionized by a well-controlled ns pulse are perfectly suited as a plasma target to drive the DLA of electrons and generate ultra-bright secondary sources of particles and radiation with high-energy, high-power sub-ps relativistic laser pulses. Experiments with foams do not demand high laser contrast or high laser pointing stability. Thin foils for proton acceleration or a thick high-Z converter for production of ultra-bright MeV bremsstrahlung, isotopes and neutrons can be attached directly to a disc containing a foam before the laser shot. These advantages were demonstrated at the 200 TW PHELIX laser[12,13,34–38].

Due to the sub-μm structure of the polymer foam, its pre-heating by the ns pulse is important in order to convert the porous matter into a homogeneous plasma for interaction with the relativistic ps pulse. In this work, we show various features of the measured electron and proton spectra caused by the different plasma profiles after exposure of the foam to the ns pulse, and discuss the results of HD simulations that take into account the porous structure of the foam and the 2D nature of the laser–foam interaction, as well as the full 3D PIC simulations that provide a better understanding of the underlying physics.

The importance of considering the foam structure and the 2D nature of the interaction with the NUTCY-F code was shown, resulting in a heating wave velocity in a foam of 2 mg/cm^3 volume density that is up to 5–10 times slower than in the case of a homogeneous substance of the same volume density and/or a 1D approach. The HD simulations performed resulted in two different types of plasma density profiles, both useful for applications: one with a density increase followed by the NCD part and the other with the bell-shaped profile of subcritical density due to the expansion of the foam in the forward and backward directions.

3D PIC simulations have shown that a smoothed density increase is favourable for DLA and leads to a higher effective temperature of accelerated electrons than in the case of a constant density plasma slab. Nevertheless, we found no significant difference between the profiles containing the NCD part in terms of total electron charge and effective temperature. These results can explain the high stability of the parameters of the DLA beam (see, e.g., Ref. [13]) and other secondary sources observed in experiments at the PHELIX facility.

The under-dense plasma target with a bell-like shape is very promising for experiments on DLA of electrons beyond GeV energies with multi-PW-class lasers.

Acknowledgements

The results presented here are based on Experiment P207 performed at the PHELIX facility at the GSI Helmholtzzentrum für Schwerionenforschung, Darmstadt, Germany, in the framework of FAIR Phase-0 in 2021. The authors are very grateful for the support provided by the PHELIX laser team. This work was funded by the German Ministry for Education and Research (BMBF) under contract No. 05P21SJFA2, by the Ministry of Science and Higher Education of the Russian Federation (Agreement No. 075-15-2021-1361), by the Czech Ministry of Education, Youth and Sports (Project No. CZ.02.2.69/0.0/0.0/18_053/0016980) and by the Grant Agency of the Czech Republic (Grant No. GM23-05027M).

Author contributions

O.N.R., M.G. and N.E.A. wrote the manuscript with revision by all co-authors, M.G., P.T., N.B., J.C. and S.Z. performed the experiment, M.G., N.B., P.K. and O.N.R. analysed the data. N.E.A, V.S.P. and A.P. performed 3D PIC simulations,

https://doi.org/10.1017/hpl.2024.85 Published online by Cambridge University Press

while R.A.Y., G.A.V. and S.Yu.G. performed 2D hydro-simulations. N.G.B., A.I.G. and V.G.P. produced polymer foam targets.

References

1. A. Pukhov, Z.-M. Sheng, and J. Meyer-ter-Vehn, Phys. Plasmas **6**, 2847 (1999).
2. A. Pukhov, Rep. Prog. Phys. **66**, 47 (2003).
3. S. P. D. Mangles, B. R. Walton, M. Tzoufras, Z. Najmudin, R. J. Clarke, A. E. Dangor, R. G. Evans, S. Fritzler, A. Gopal, C. Hernandez-Gomez, W. B. Mori, W. Rozmus, M. Tatarakis, A. G. R. Thomas, F. S. Tsung, M. S. Wei, and K. Krushelnick, Phys. Rev. Lett. **94**, 245001 (2005).
4. F. Albert, N. Lemos, J. L. Shaw, P. M. King, B. B. Pollock, C. Goyon, W. Schumaker, A. M. Saunders, K. A. Marsh, A. Pak, J. E. Ralph, J. L. Martins, L. D. Amorim, R. W. Falcone, S. H. Glenzer, J. D. Moody, and C. Joshi, Phys. Plasmas **25**, 056706 (2018).
5. P. M. King, K. Miller, N. Lemos, J. L. Shaw, B. F. Kraus, M. Thibodeau, B. M. Hegelich, J. Hinojosa, P. Michel, C. Joshi, K. A. Marsh, W. Mori, A. Pak, A. G. R. Thomas, and F. Albert, Phys. Rev. Accel. Beams **24**, 011302 (2021).
6. M. A. Stoyer, T. C. Sangster, E. A. Henry, M. D. Cable, T. E. Cowan, S. P. Hatchett, M. H. Key, M. J. Moran, D. M. Pennington, M. D. Perry, T. W. Phillips, M. S. Singh, R. A. Snavely, M. Tabak, and S. C. Wilks, Rev. Sci. Instrum. **72**, 767 (2001).
7. H. Chen, A. Link, Y. Sentoku, P. Audebert, F. Fiuza, A. Hazi, R. F. Heeter, M. Hill, L. Hobbs, A. J. Kemp, G. E. Kemp, S. Kerr, D. D. Meyerhofer, J. Myatt, S. R. Nagel, J. Park, R. Tommasini, and G. J. Williams, Phys. Plasmas **22**, 056705 (2015).
8. D. Raffestin, L. Lecherbourg, I. Lantuéjoul, B. Vauzour, P. E. Masson-Laborde, X. Davoine, N. Blanchot, J. L. Dubois, X. Vaisseau, E. d'Humières, L. Gremillet, A. Duval, Ch. Reverdin, B. Rosse, G. Boutoux, J. E. Ducret, Ch. Rousseaux, V. Tikhonchuk, and D. Batani, Matter Radiat. Extremes **6**, 056901 (2021).
9. L. Willingale, A. G. R. Thomas, P. M. Nilson, H. Chen, J. Cobble, R. S. Craxton, A. Maksimchuk, P. A. Norreys, T. C. Sangster, R. H. H. Scott, C. Stoeckl, C. Zulick, and K. Krushelnick, New J. Phys. **15**, 025023 (2013).
10. A. E. Hussein, A. V. Arefiev, T. Batson, H. Chen, R. S. Craxton, A. S. Davies, D. H. Froula, Z. Gong, D. Haberberger, Y. Ma, P. M. Nilson, W. Theobald, T. Wang, K. Weichman, G. J. Williams, and L. Willingale, New J. Phys. **23**, 023031 (2021).
11. L. Willingale, A.V. Arefiev, G. J. Williams, H. Chen, F. Dollar, A. U. Hazi, A. Maksimchuk, M. J.-E. Manuel, E. Marley, W. Nazarov, T. Z. Zhao, and C. Zulick, New J. Phys. **20**, 093024 (2018).
12. O. N. Rosmej, N. E. Andreev, S. Zaehter, N. Zahn, P. Christ, B. Borm, T. Radon, A. Sokolov, L. P. Pugachev, D. Khaghani, F. Horst, N. G. Borisenko, G. Sklizkov, and V. G. Pimenov, New J. Phys. **21**, 043044 (2019).
13. O. N. Rosmej, M. Gyrdymov, M. M. Günther, N. E. Andreev, P. Tavana, P. Neumayer, S. Zähter, N. Zahn, V. S. Popov, N. G. Borisenko, A. Kantsyrev, A. Skobliakov, V. Panyushkin, A. Bogdanov, F. Consoli, X. F. Shen, and A. Pukhov, Plasma Phys. Control. Fusion **62**, 115024 (2020).
14. L. P. Pugachev, N. E. Andreev, P. R. Levashov, and O. N. Rosmej, Nucl. Instrum. Methods A **829**, 88 (2016).
15. L. P. Pugachev and N. E. Andreev, J. Phys.: Conf. Ser. **1147**, 012080 (2019).
16. J. H. Bin, M. Yeung, Z. Gong, H. Y. Wang, C. Kreuzer, M. L. Zhou, M. J. V. Streeter, P. S. Foster, S. Cousens, B. Dromey, J. Meyer-ter-Vehn, M. Zepf, and J. Schreiber, Phys. Rev. Lett. **120**, 074801 (2018).
17. Y. Shou, P. Wang, S. G. Lee, Y. J. Rhee, H. W. Lee, J. W. Yoon, J. H. Sung, S. K. Lee, Z. Pan, D. Kong, Z. Mei, J. Liu, S. Xu, Z. Deng, W. Zhou, T. Tajima, I. W. Choi, X. Yan, C. Hee Nam, and W. Ma, Nat. Photonics **17**, 137 (2022).
18. N. E. Andreev, V. S. Popov, O. N. Rosmej, A. A. Kuzmin, A. A. Shaykin, E. A. Khazanov, A. V. Kotov, N. G. Borisenko, M. V. Starodubtsev, and A. A. Soloviev, Quantum Electron. **51**, 1019 (2021).
19. N. E. Andreev, I. R. Umarov, and V. S. Popov, Bull. Lebedev Phys. Inst. **50**, 797 (2023).
20. R. Huang, L. Han, Y. Shou, D. Wang, T. Yu, J. Yu, and X. Yan, Opt. Lett. **48**, 819 (2023).
21. A. M. Khalenkov, N. G. Borisenko, V. N. Kondrashov, Yu. A. Merkuliev, J. Limpouch, and V. G. Pimenov, Laser Part. Beams **24**, 283 (2006).
22. N. G. Borisenko, A. M. Khalenkov, V. Kmetik, J. Limpouch, Yu. A. Merkuliev, and V. G. Pimenov, Fusion Sci. Technol. **51**, 655 (2007).
23. N. G. Borisenko, A. A. Akunets, L. A. Borisenko, A. I. Gromov, A. S. Orekhov, A. V. Pastukhov, V. G. Pimenov, S. M. Tolokonnikov, and G. V. Sklizkov, J. Phys.: Conf. Ser. **1692**, 012026 (2020).
24. O. N. Rosmej, N. Suslov, D. Martsovenko, G. Vergunova, N. Borisenko, N. Orlov, T. Rienecker, D. Klir, K. Rezack, and A. Orekhov, Plasma Phys. Control. Fusion **57**, 094001 (2015).
25. S. N. Chen, T. Iwawaki, K. Morita, P. Antici, S. D. Baton, F. Filippi, H. Habara, M. Nakatsutsumi, P. Nicolaï , W. Nazarov, C. Rousseaux, M. Starodubstev, K. A. Tanaka, and J. Fuchs, Sci. Rep. **6**, 21495 (2016).
26. S. Yu. Gus'kov, A. Caruso, V. B. Rozanov, and C. Strangio, Quantum Electron. **30**, 191 (2000).
27. S. Yu. Gus'kov, J. Limpouch, Ph. Nicolaï, and V. T. Tikhonchuk, Phys. Plasmas **18**, 103114 (2011).
28. S. Depierreux, C. Labaune, D. T. Michel, C. Stenz, P. Nicolai, M. Grech, G. Riazuelo, S. Weber, C. Riconda, V. T. Tikhonchuk, P. Loiseau, N. G. Borisenko, W. Nazarov, S. Huller, D. Pesme, M. Casanova, J. Limpouch, C. Meyer, P. Di-Nicola, R. Wrobel, E. Alozy, P. Romary, G. Thiell, G. Soullie, C. Reverdin, and B. Villette, Phys. Rev. Lett. **102**, 195005 (2009).
29. J. Colvin, H. Matsukuma, K. Brown, J. Davis, G. Kemp, K. Koga, N. Tanaka, A. Yogo, Z. Zhang, H. Nishimura, and K. Fournier, Phys. Plasmas **25**, 032702 (2018).
30. O. S. Jones, G. E. Kemp, S. H. Langer, B. J. Winjum, R. L. Berger, J. S. Oakdale, M. A. Belyaev, J. Biener, M. M. Biener, D. A. Mariscal, J. L. Milovich, M. Stadermann, P. A. Sterne, and S. C. Wilk, Phys. Plasmas **28**, 022709 (2021).
31. V. Bagnoud, B. Aurand, A. Blazevic, S. Borneis, C. Bruske, B. Ecker, U. Eisenbarth, J. Fils, A. Frank, E. Gaul, S. Goette, C. Haefner, T. Hahn, K. Harres, H.-M. Heuck, D. Hochhaus, D. H. H. Hoffmann, D. Javorková, H.-J. Kluge, T. Kuehl, S. Kunzer, M. Kreutz, T. Merz-Mantwill, P. Neumayer, E. Onkels, D. Reemts, O. Rosmej, M. Roth, T. Stoehlker, A. Tauschwitz, B. Zielbauer, D. Zimmer, and K. Witte, Appl. Phys. B **100**, 137 (2010).
32. J. Ren, Z. Deng, W. Qi, B. Chen, B. Ma, X. Wang, S. Yin, J. Feng, W. Liu, Z. Xu, D. H. H. Hoffmann, S. Wang, Q. Fan, B. Cui, S. He, Z. Cao, Z. Zhao, L. Cao, Y. Gu, S. Zhu, R. Cheng, X. Zhou, G. Xiao, H. Zhao, Y. Zhang, Z. Zhang, Y. Li, D. Wu, and W. Zhou, Nat. Commun. **11**, 5157 (2020).
33. X. F. Shen, A. Pukhov, M. M. Günther, and O. N. Rosmej, Appl. Phys. Lett. **118**, 134102 (2021).

https://doi.org/10.1017/hpl.2024.85 Published online by Cambridge University Press

34. O. N. Rosmej, X. F. Shen, A. Pukhov, L. Antonelli, F. Barbato, M. Gyrdymov, M. M. Günther, S. Zähter, V. S. Popov, N. G. Borisenko, and N. E. Andreev, Matter Radiat. Extremes **6**, 048401 (2021).
35. J. Cikhardt, M. Gyrdymov, S. Zähter, P. Tavana, M. M. Günther, N. Bukharskii, N. Borisenko, J. Jacoby, X. F. Shen, A. Pukhov, N. E. Andreev, and O. N. Rosmej, Matter Radiat. Extremes **9**, 027201 (2024).
36. M. Gyrdymov, J. Cikhardt, P. Tavana, N. G. Borisenko, S. Yu. Gus'kov, R. A. Yakhin, G. A. Vegunova, W. Wei, J. Ren, Y. Zhao, D. H. H. Hoffmann, Z. Deng, W. Zhou, R. Cheng, J. Yang, J. Novotny, X. Shen, A. Pukhov, J. Jacoby, C. Spielmann, V. S. Popov, M. E. Veysman, N. E. Andreev, and O. N. Rosmej, Sci. Rep. **14**, 14785 (2024).
37. M. M. Günther, O. N. Rosmej, P. Tavana, M. Gyrdymov, A. Skobliakov, A. Kantsyrev, S. Zähter, N. G. Borisenko, A. Pukhov, and N. E. Andreev, Nat. Commun. **13**, 170 (2022).
38. P. Tavana, N. Bukharskii, M. Gyrdymov, U. Spillmann, Ş. Zähter, J. Cikhardt, N. G. Borisenko, Ph. Korneev, J. Jacoby, C. Spielmann, N. E. Andreev, M. M. Günther, and O. N. Rosmej, Front. Phys. **11**, 1178967 (2023).
39. S. Yu. Gus'kov and V. B. Rozanov, Quantum Electron. **27**, 696 (1997).
40. G. A. Vergunova, V. B. Rosanov, O. B. Denisov, N. Yu. Orlov, and O. N. Rosmej, Plasma Emission **39**, 755 (2013).
41. T. Bonnet, M. Comet, D. Denis-Petit, F. Gobet, F. Hannachi, M. Tarisien, M. Versteegen, and M. M. Aléonard, Rev. Sci. Instrum. **84**, 103510 (2013).
42. S. Yu. Gus'kov and R. A. Yakhin, Matter Radiat. Extremes **9**, 016601 (2024).
43. S. Yu. Gus'kov, M. Cipriani, R. De Angelis, F. Consoli, A. A. Rupasov, P. Andreoli, G. Cristofari, and G. Di Giorgio, Plasma Phys. Control. Fusion **57**, 125004 (2015).
44. S. Yu. Gus'kov and R. A. Yakhin, Phys. Plasmas **30**, 062709 (2023).
45. V. B. Rozanov and G. A. Vergunova, J. Exp. Theor. Phys. **121**, 747 (2015).
46. J. Denavit and D. W. Phillion, Phys. Plasmas **1**, 1971 (1994).
47. S. Yu. Gus'kov, P. A. Kuchugov, and R. A. Yakhin, Phys. Plasmas **28**, 092108 (2021).
48. A. Pukhov, J. Plasma Phys. **61**, 425 (1999).
49. C. E. Max, J. Arons, and A. B. Langdon, Phys. Rev. Lett. **33**, 209 (1974).
50. A. Pukhov and J. Meyer-ter-Vehn, Phys. Rev. Lett. **76**, 3975 (1996).
51. M. Borghesi, A. J. MacKinnon, L. Barringer, R. Gaillard, L. A. Gizzi, C. Meyer, O. Willi, A. Pukhov and J. Meyer-ter-Vehn, Phys. Rev. Lett. **78**, 879 (1997).
52. R. Babjak, B. Martinez, M. Krus, and M. Vranic, New J. Phys **26**, 093002 (2024).
53. D. R. Rusby, A. J. Kemp, S. C. Wilks, K. G. Miller, M. Sherlock, H. Chen, R. A. Simpson, D. A. Mariscal, K. Swanson, B. Z. Djordjevi, A. J. Link, G. J. Williams, and A. J. Mackinnon, Phys. Plasmas **31**, 040503 (2024).
54. R. Babjak, L. Willingale, A. Arefiev, and M. Vranic, Phys. Rev. Lett. **132**, 125001 (2024).
55. A. B. Borisov, O. B. Shiryaev, A. McPherson, K. Boyer, and C. K. Rhodes, Plasma Phys. Control. Fusion **37**, 569 (1995).
56. T. W. Huang, C. T. Zhou, A. P. L. Robinson, B. Qiao, H. Zhang, S. Z. Wu, H. B. Zhuo, P. A. Norreys, and X. T. He, Phys. Rev. E **92**, 053106 (2015).
57. X. F. Shen, A. Pukhov, O. N. Rosmej, and N. E. Andreev, Phys. Rev. Appl. **18**, 064091 (2022).
58. H. Tang, K. Tangtartharakul, R. Babjak, I.-L. Yeh, F. Albert, H. Chen, P. T. Campbell, Y. Ma, P. M. Nilson, B. K. Russell, J. L. Shaw, A. G. R. Thomas, M. Vranic, A. V. Arefiev, and L. Willingale, New J. Phys. **26**, 053010 (2024).

https://doi.org/10.1017/hpl.2024.85 Published online by Cambridge University Press